

Geometric Phase Optics

B. Zygelman*

Department of Physics and Astronomy, University of Nevada, Las Vegas, Las Vegas NV 89154

(Dated: May 14, 2022)

We introduce, and propagate wave-packet solutions of, a single qubit system in which geometric gauge forces and phases emerge. We investigate under what conditions non-trivial gauge phenomena arise, and demonstrate how symmetry breaking is an essential ingredient for realization of the former. We illustrate how a “magnetic”-lens, for neutral atoms, can be constructed and find application in the manipulation and interferometry of cold atoms.

PACS numbers: 03.65.-w,03.65.Aa,03.65.Nk,03.65.Vf,34.30.Cf

INTRODUCTION

Gauge symmetry is at the core of our current understanding of how the fundamental constituents of matter interact. With the discovery of the geometric phase[1] diverse systems, ranging atomic, molecular, optical, condensed matter and nuclear physics, have been identified in which gauge phenomena, in addition to those arising from fundamental gauge fields, emerge. More recently, researchers[2] have, via the application of laser fields on cold atoms, engineered Hamiltonians that lead to effective “magnetic”-like forces on the atoms. This advance has great potential in the control and manipulation of quantum matter[3]. In particular, its application promises the capability to create ensembles of neutral atoms that exhibit exotic quantum Hall-like behavior[4, 5].

In this Letter, we introduce a single qubit model that possesses non-trivial gauge behavior and whose laboratory realization may offer novel routes to the quantum control, and interferometry, of cold atoms. We present results of time-dependent calculations for wave-packet propagation to illustrate how, and under what conditions, geometric gauge forces manifest. We show how the proposed system mimics that of a charged particle scattered by a ferromagnetic medium. We illustrate how an effective “magnetic” lens can be engineered and propose possible applications.

THEORY

Consider the Hamiltonian

$$H = -\frac{\hbar^2}{2m} \nabla^2 + H_{ad}(\mathbf{R}) \quad (1)$$

where $H_{ad}(\mathbf{R})$, the adiabatic Hamiltonian describing a qubit, is parameterized by the quantum variable \mathbf{R} , and which can be expressed in the form

$$H_{ad} = U(\mathbf{R})H_{BO}U^\dagger(\mathbf{R}). \quad (2)$$

A detailed, time-independent, description of such systems has been outlined in Ref. [6], but here we exploit time-dependent methods to enhance and generalize the conclusions of that paper. Laboratory realizations of adiabatic Hamiltonians discussed in this Letter could be

achieved using the techniques discussed in Refs. [3, 4]. Because U is a unitary operator the eigenvalues of H_{ad} are solely determined by H_{BO} that, in this study, we require to be non-degenerate. We take the eigenstates of H_{BO} as our basis and set $H_{BO} = \Delta \sigma_3$ where $\Delta > 0$ is a constant and σ_3 is the diagonal Pauli matrix. We choose[6] for U ,

$$\exp(-i\sigma_3 \frac{\Phi}{2} y) \exp(-i\sigma_2 \Omega(x)) \exp(i\sigma_3 \frac{\Phi}{2} y) \quad (3)$$

where σ_i are the Pauli matrices, Φ is a parameter, $\mathbf{R} = (x, y)$ are 2D Cartesian coordinates, and

$$\Omega(x) = \frac{\pi}{4} \left(1 + \tanh(\beta x) \right). \quad (4)$$

We seek solutions of $i\hbar \partial_t \psi(\mathbf{R}) = H\psi(\mathbf{R})$ which, expressed in this basis, take the form of the coupled equations

$$\begin{aligned} i\hbar \frac{\partial f}{\partial t} &= -\frac{\hbar^2}{2m} \nabla^2 f + V f + V_{12}g \\ i\hbar \frac{\partial g}{\partial t} &= -\frac{\hbar^2}{2m} \nabla^2 g + V_{12}^* f - V g \end{aligned} \quad (5)$$

where

$$\begin{aligned} \psi &\equiv \begin{pmatrix} f \\ g \end{pmatrix} \\ V &= \Delta \cos(2\Omega(x)) \\ V_{12} &= \exp(-i\Phi y) \Delta \sin(2\Omega(x)). \end{aligned} \quad (6)$$

They may be solved using the split-operator method[7], and a wave packet at $t = t_0$, can be propagated to $t = t_0 + \delta t$, for a small time increment δt . Introducing the dimensionless units $\tau = \frac{L^2}{2m\hbar} t$, $(\xi, \eta) = (x/L, y/L)$, where L is an arbitrary length scale, we obtain

$$\psi(\tau + \delta\tau) = U_{KE} U_V U_{KE} \psi(\tau) \quad (7)$$

where U_{KE} is a diagonal matrix operator whose elements are,

$$\exp\left(i \frac{\delta\tau}{2} \left(\frac{\partial^2}{\partial \xi^2} + \frac{\partial^2}{\partial \eta^2} \right)\right)$$

and

$$U_V = \begin{pmatrix} \cos(\Delta \delta\tau) - i \cos(2\Omega(\xi)) \sin(\Delta \delta\tau) & -i \exp(-i\Phi \eta) \sin(2\Omega(\xi)) \sin(\Delta \delta\tau) \\ -i \exp(i\Phi \eta) \sin(2\Omega(\xi)) \sin(\Delta \delta\tau) & \cos(\Delta \tau) + i \cos(2\Omega(\xi)) \sin(\Delta \delta\tau) \end{pmatrix}.$$

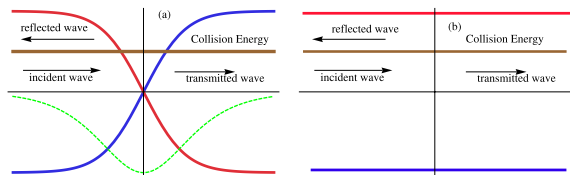


FIG. 1: (a) An incident wave in the open channel whose potential energy is given by the solid blue line. For $\xi > 0$ the transmitted wave is propagated on the potential surface given by the red solid line. The brown line represent the total collision energy of the system and the green dashed line represents the off-diagonal coupling between the two potential surfaces. (b) The same system now illustrated in the adiabatic picture (gauge). The blue line is the BO energy for the open channel and the red line represents the BO energy for the closed channel.

Expressed in these units Δ is a dimensionless parameter as are Φ, β . Figure (1) provides a schematic description of the dynamics generated by Hamiltonian (1). In Figure (2a) we provide a time series contour plot of the probability densities $|f|^2$ and $|g|^2$. At $\tau = 0$ we place a Gaussian wave-packet $\psi_0 = \begin{pmatrix} 0 \\ g_0 \end{pmatrix}$ centered $\xi = -4.0$, $\eta = 0$ with an initial velocity directed along the positive ξ axis. In this region ($\Omega \rightarrow 0$)

$$H_{ad} = \begin{pmatrix} \Delta & 0 \\ 0 & -\Delta \end{pmatrix}$$

and the wave packet evolves as that of a free particle until it reaches the interaction region $\xi \approx 0$. The wave-packet is illustrated by the blue contours in Figure (2a). The initial kinetic energy of the packet was chosen so penetration of the potential barrier, illustrated in Figure (1), is prevented. However, the packet can execute a transition into the open channel across the barrier. In other words, a transition from the g to f channel occurs in the region $\xi \approx 0$. This is illustrated in Figure (2a) by the red contours that represent the wave-packet, probability, contours in the f channel. In addition to distortion and spreading of the packet there is a noticeable swerve in its velocity as it emerges from the interaction region.

We define the adiabatic amplitudes,

$$\begin{aligned} \tilde{f} &= f \cos \Omega(\xi) + \exp(-i\Phi \eta) \sin \Omega(\xi) g \\ \tilde{g} &= g \cos \Omega(\xi) - \exp(i\Phi \eta) \sin \Omega(\xi) f \end{aligned} \quad (8)$$

and $\tilde{\psi} = \begin{pmatrix} \tilde{f} \\ \tilde{g} \end{pmatrix}$ obeys the following equation[6]

$$i\hbar \frac{\partial \tilde{\psi}}{\partial t} = -\frac{\hbar^2}{2m} (\nabla - i\mathbf{A})^2 \tilde{\psi} + H_{BO} \tilde{\psi}, \quad (9)$$

where \mathbf{A} is a non-Abelian, pure, gauge potential. In the region $\xi \rightarrow -\infty$, $\Omega \rightarrow 0$ and $\tilde{g} \rightarrow g$. Likewise as $\xi \rightarrow \infty$, $\Omega \rightarrow \pi/2$ and $\tilde{g} \rightarrow f$. This behavior is illustrated in Figure (2b) where we present a 3D plot for the evolution of $|\tilde{g}|^2$. In the adiabatic picture the open channel amplitude \tilde{g} evolves in a constant adiabatic potential $-\Delta$ shown in Figure (1b). As long as the collision energy is below the threshold for excitation into the upper adiabatic, or closed, channel the system evolves on a single adiabatic surface. Under such conditions the Born-Oppenheimer (BO) approximation to the solutions of Eq. (9) is appropriate. In this approximation, the projection operator $P\tilde{\psi} = \tilde{g}$, is applied on Eq. (9) to get

$$i\hbar \frac{\partial \tilde{g}}{\partial t} = -\frac{\hbar^2}{2m} (\nabla - i\tilde{\mathbf{A}})^2 \tilde{g} - \left(\Delta - \frac{\hbar^2 b(x)}{2m} \right) \tilde{g} \quad (10)$$

where $\tilde{\mathbf{A}} = P\mathbf{A}P$ is an Abelian gauge potential with non-vanishing curl and $b(x)$ is an induced scalar potential[6]. It leads to an effective magnetic induction

$$|\mathbf{B}(\xi)| = \frac{\pi}{4} \beta \Phi \operatorname{sech}^2(\beta\xi) \cos\left(\frac{\pi}{2} \tanh(\beta\xi)\right) \quad (11)$$

and mimics that incurred on a charged particle that is scattered by a ferromagnetic medium. The magnetic induction is normal to the plane of the page, and is illustrated by the green shaded area in Figure (2b). In Figure (2a) we also plot, shown by the dashed line, the trajectory for the solution of the classical equations of motion, subjected to a Lorentz force $\mathbf{v} \times \mathbf{B}$, where $|\mathbf{B}|$ is given by Eq. (11). Comparison of the classical path and that traced by the centers of the wave-packets shows good agreement. The deflection angle suffered by a charged particle that is normally incident on a ferromagnetic slab, of finite width, with constant magnetic induction \mathbf{B} directed perpendicular to the plane of the page is[6],

$$\tan \theta = \frac{|\Phi|}{\sqrt{k^2 - \Phi^2}} \quad (12)$$

where $\Phi = \int_{-\infty}^{\infty} d\xi B(\xi)$ is a flux density, and k the incident wave number.

In Table I we tabulate values of the deflection angles θ , obtained by calculating the expectation values $\langle \xi(t) \rangle$, $\langle \eta(t) \rangle$ for various values of incident, adiabatic, packet wave numbers k and Φ . In that table we show the dependence of θ on the choice of the energy gap parameter Δ . At lower collision energies, so that $k^2 \ll 2\Delta$, we

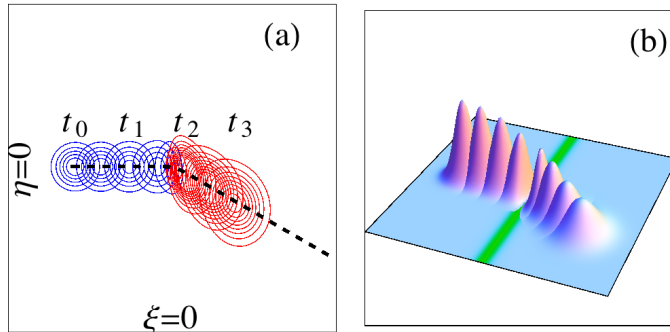


FIG. 2: (a) Blue contours represent the initial g component of the wave packet probability distribution. At time t_2 the packet executes a transition into the f channel, shown by the red contours, which is energetically open in the region $\xi > 0$. Subsequent to the transition the packet evolves as a free particle but with a pronounced swerve in its velocity. (b) 3D plot of the adiabatic gauge probability distribution $|\tilde{g}(t)|^2$. In both figures the deflection angle has the value $\tan \theta \approx 0.59$. In these calculations we took $k = 12, \Phi = 6, \Delta = 200, \beta = 2$ and $\tau_0 = 0, \tau_1 = 20, \tau_2 = 30, \tau_3 = 40$. ξ, η range between $\mp 2\pi$.

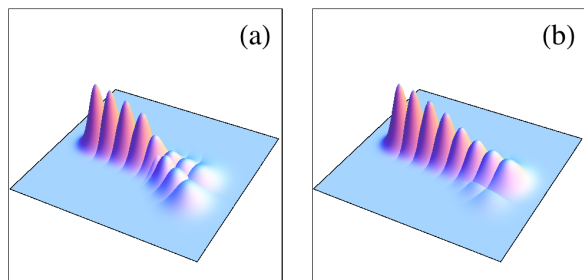


FIG. 3: Plot of probability densities $|g|^2, |f|^2$ when both channels are open. The threshold energy $k_t^2 = 2\Delta$. (a) $k^2 = 3k_t^2$. (b) $k^2 = 6k_t^2$.

find that Eq. (12) provides a good approximation for θ . As the energy gap 2Δ is decreased, for a fixed value of k , Eq. (12) is less accurate. However, even at threshold $k^2 \approx 2\Delta$ there is still fairly good agreement between the calculated value and that predicted by solutions of Eq. (10). When $k^2 > 2\Delta$ the excited adiabatic state is open and transitions from the adiabatic channel labeled \tilde{g} into \tilde{f} is energetically allowed. In Figure (3a) we illustrate the evolution of the amplitudes $|g(t)|^2$ and $|f(t)|^2$ for the collision energy where $2\Delta/k^2 = 1/3$. The incident packet, in the g channel, bifurcates when it reaches the interaction region. Because there is sufficient kinetic energy, the remainder of the initial packet proceeds along the path $\eta = 0$ in the region $\xi > 0$. However, a fraction of that packet makes a transition into the f channel, and our calculations show that the angle of the swerve illustrated in that figure is in harmony with that obtained at the lower collision energies tabulated in Table I. Therefore there is a state-dependent spatial segregation of the initial beam, a hallmark of quantum control. In panel (b) of that figure we plot these probabilities for energies $2\Delta/k^2 = 1/6$

TABLE I: Calculated values for the deflection angle θ are tabulated in the third column. The fourth column gives the values obtained using Eq. (12)

$2\Delta/k^2$	Φ/k	$\tan \theta$	$\tan \theta_c$
25/9	1/2	0.587	0.577
25/9	1/4	0.270	0.258
25/9	1/12	0.088	0.084
1	1/2	0.63	0.577
1	1/4	0.269	0.258
1	1/12	0.088	0.084

and now find a small, barely noticeable, remnant of the packet in the f channel. In the limit $k \rightarrow \infty$ (or $\Delta \rightarrow 0$) Eq. (5) allow analytic solutions and $g(t)$ simply evolves as that of a free particle. According to definition Eq. (8) the initial, adiabatic gauge, packet $\tilde{g}(t)$ makes a transition into the \tilde{f} channel in the region $\xi > 0$. This "transition" is induced by the off-diagonal gauge couplings in Eq. (9). The "transition" is simply an artifact of the adiabatic gauge (i.e. different definitions for the scattering basis in the two asymptotic regions, $\xi < 0, \xi > 0$) and does constitute a "real" physical transition. In order to better understand the behavior illustrated above we re-express the unitary operator U that defines the adiabatic Hamiltonian. In Ref. [6] we argued that U can always be written in the form

$$U(\mathbf{R}) = \mathcal{P} \exp(-i \int_{\mathcal{C}}^{\mathbf{R}} d\mathbf{R}' \cdot \mathbf{A}) \quad (13)$$

where \mathcal{P} is a path ordering operator, and \mathbf{A} is a non-Abelian gauge potential. U must be well-defined (i.e. not multi-valued) for all \mathbf{R} and therefore Eq. (13) must be independent of the path \mathcal{C} , or $\mathcal{P} \exp(-i \oint d\mathbf{R}' \cdot \mathbf{A}) = 1$. Gauge potentials that satisfy this condition are sometimes called a pure gauge and typically have vanishing

curvature everywhere. Because of relation (13) we conclude that \mathbf{A} is encoded in the definition of H_{ad} and since $[H_{BO}, \mathbf{A}] \neq 0$ gauge symmetry is explicitly broken by H_{BO} . Though \mathbf{A} is trivial, in the sense of it being a pure gauge, quantum evolution selects and is sensitive to the projected $\tilde{\mathbf{A}} = PAP$ non-trivial connection. In the adiabatic picture the gauge potentials are explicit, being minimally coupled to the amplitudes. As $k \rightarrow \infty$, or $\Delta \rightarrow 0$, their presence simply contributes to a multichannel, or non-Abelian, phase in the adiabatic amplitudes that has no physical import. In contrast, at lower energies the system behaves as if it has acquired a non-integrable phase factor. The effect is most pronounced when the excited adiabatic state is closed.

APPLICATIONS

In the discussion up to this point, we have used time-dependent methods to validate and extend the conclusions given in Ref. [6] in which time-independent methods allow exact scattering solutions for Hamiltonian (1). However, time dependent methods can be exploited for more complex scattering scenarios. Following an analysis similar to that in which Eq. (12) was derived, we now posit the following form for the parameter

$$\Phi(\eta) = \frac{\eta k}{\sqrt{\eta^2 + 4\gamma f^2}} \quad (14)$$

where γ is, in general, a complicated function of β, k, Δ . Here we set it to have the constant value $\gamma = 1$. Using Eq. (14) we propagate wave packets for various values of impact parameter. In Figure (4 a) we plot trajectories of the total expectation values $\langle \psi(t) | \xi | \psi(t) \rangle$, $\langle \psi(t) | \eta | \psi(t) \rangle$ for the various impact parameters b . At each impact parameter we choose identical wave-packet widths and set $k = 12, \Delta = 400$. The trajectories shown in that figure, by the solid red lines, demonstrate that the paths converge to a common focal point given by $f = 3$. This result is gauge invariant, i.e. it can be obtained using amplitudes obtained in either diabatic or adiabatic gauges. However, the adiabatic picture provides a transparent physical description. For, in it, the system is accurately described by Eq. (10). That description includes the emergence of an effective magnetic induction $\mathbf{B} = \nabla \times \tilde{\mathbf{A}}$ whose magnitude is

$$\frac{\pi\beta k\eta (8f^2 + \eta^2) \operatorname{sech}^2(\beta\xi) \cos(\frac{1}{2}\pi \tanh(\beta\xi))}{4(4f^2 + \eta^2)^{3/2}} \quad (15)$$

and is normal to the plane of the page. In Figure (4b) we illustrate the propagation of a coherent wave packet slab of finite width along the η direction. After its passage through the “magnetic” lens at $\xi \approx 0$, its shape is

significantly distorted. At $\tau_1 = 30$, where the packet describes free particle evolution, it assumes the shape of a “shark-fin” as shown in that figure. The width, along the η direction, is significantly reduced from its value at τ_0 . A dramatic consequence of the proposed “magnetic” lensing effect. Such a lens, if realized, could find application as an “optical” component in an atom laser. In addition, consider two localized but coherent packets spatially separated at $t = 0$. After passing through the lens they meet and interfere. Because of different geometric phase histories the interference pattern depends on the “magnetic” flux enclosed by the paths. One can therefore anticipate its application as a novel expression of atom interferometry.

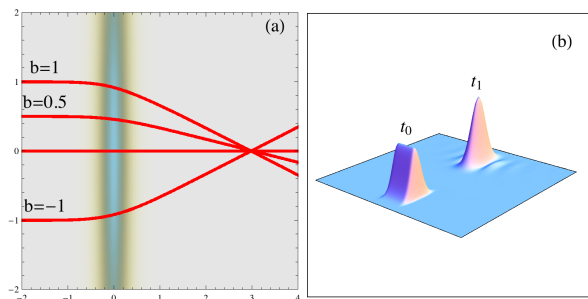


FIG. 4: (a) Trajectories of wave-packet expectation values for various values of impact parameter. The shaded region is a density plot of Eq. (15) for the “magnetic” induction. (b) A wave packet slab having width $d = 2$ along the η axis at $\tau_0 = 0$ is propagated to the position shown at $\tau_1 = 30$.

* bernard@physics.unlv.edu

- [1] A. Shapere and F. Wilczek, *Geometric Phases in Physics* (World Scientific Publishing Company, 1989).
- [2] Y. Lin, R. L. Compton, A. R. Perry, W. D. Phillips, J. V. Porto, and I. B. Spielman, *Physical Review Letters* **102**, 130401 (2009).
- [3] J. Dalibard, F. Gerbier, G. Juzeliūnas, and P. Öhberg, *Reviews of Modern Physics* **83**, 1523 (2011).
- [4] B. Juliá-Díaz, D. Dagnino, K. J. Günter, T. Graß, N. Barberán, M. Lewenstein, and J. Dalibard, *Phys. Rev. A* **84**, 053605 (2011).
- [5] I. B. Spielman, *Nature* **472**, 301 (2011).
- [6] B. Zygelman, *ArXiv e-prints* (2012), arXiv:1202.2908 [quant-ph].
- [7] M. R. Hermann and J. A. Fleck, Jr., *Phys. Rev. A* **38**, 6000 (1988).